Electrochemical Properties of Deactivated CuOx/Active Carbon Catalyst

Hanqing Zhao[1], Liqin Wang[1], Shoudong Xu[2], Ding Zhang[2], Guoqiang Zhang[1],
Shibin Liu[2] and Zhong Li[1,]*

[1] Key Laboratory of Coal Science and Technology of Ministry of Education and Shanxi Province, Institute of Coal Chemical Engineering, Taiyuan University of Technology, Taiyuan 030024, Shanxi, China
[2] College of Chemistry and Chemical Engineering, Taiyuan University of Technology, Taiyuan 030024, Shanxi, China
[*]E-mail: lizhong@tyut.edu.cn

Low-cost and high-performance electrodes are desired for energy storage devices such as lithium-ion (Li-ion) batteries. In this work, CuO_x/active carbon (CuO_x/AC), originated from the deactivated catalyst for synthesizing dimethyl carbonate (DMC), was characterized as Li-ion battery anodes. Various copper valences (Cu^0, Cu^+ and Cu^{2+}) exist on the surface and inside of the nanoparticle catalyst. After simple heat-treatment, the sample exhibits a storage capacity of 621.3 mAh•g^{-1} after 100 cycles at a current density of 100 mA•g^{-1}, which changes to 359.6 mAh•g^{-1} at a high current density of 1 A•g^{-1} after 500 cycles. This excellent behaviour can be ascribed to synergetic effect of CuO_x nanoparticles/actived carbon support and CuO/Cu_2O, which can synergistically strengthen the intrinsic properties of each component. Additionally, functional groups on AC surface can promote Li-ion storage performance. This work shows good electrochemical properties and potential application of CuO_x/AC deactivated catalyst as Li-ion battery anodes.

1. INTRODUCTION

The traditional carbon based materials, being considered as the popular material for making the electrodes, have disadvantages of low theoretical capacity (372 mAh·g^{-1}) and are vulnerable to passivation [1]. As one type of 3*d* transition-metal oxides, cuprous oxide (Cu_2O) and cupric oxide (CuO) are *p*-type semiconductors with low band-gap energy and nontoxic nature with theoretical

capacities of 375 and 674 mAh g^{-1} [2]. Copper oxides have been recently suggested as a suitable anode material for LIBs, thanks to the types of redox reactions among different Cu ions, which result in high specific capacities and show multiple times higher capacity than that of carbon/graphite-based materials [3]. Nevertheless, CuO_x anodes are limited by the reversible of electrode reaction decline and the fast capacity decaying. This is caused by large volume inflation and falling off of the active materials during repeated charge/discharge processes [4].

In order to overcome the drawbacks above and improve electrochemical performance of materials, CuO_x with various morphologies such as octahedra[5], hollow [6], nanoflake arrays [7] and nano-needle arrays[8] have been implemented. Although these nano-sized materials have advantages of high specific surface area, weakened volume expansion and short path length to facilitate Li-ion diffusion, it still remains a great challenge for future commercial application owing to the high cost and complicated process.

CuO_x/AC composites also can deliver a Li-ion storage performance, and meanwhile, copper based oxides can be applied to catalyzed synthesis DMC, which is prototype example of eco-friendly solvent and widely applied in lithium-ion batteries (LIBs) [9]. The deactivated catalysts of CuO_x/AC can be recycle utilized as anode materials of LIBs, considering the environmental friendliness and economic benefits. Electrochemical reactivity for lithium ion storage of nano-sized copper oxide particle was reported by Tarascon' group [10], which provide a scientific basis for this purpose. The mechanism for lithium storage of copper oxide is primarily based on conversion reaction involving the formation and decomposition of Li_2O along with the reduction and oxidation of CuO. In the composite, active carbon is served as a carrier exhibiting several advantages such as inertness, large surface area, and porous structure [11]. Meanwhile, the composite can realize synergistic effect, by integrating CuO_x and AC, CuO and Cu_2O, which can enhance the intrinsic properties of each component. The introducing of oxygen-containing functional groups can provide more active sites for Li-ion storage and promote the redox reaction of copper oxide. Therefore, the electrodes of these materials present remarkable electrochemical properties.

In this work, we test CuO_x/AC nanomaterial derived from deactivated catalyst from the DMC synthesis, to lithium-ion battery anodes after simple heat treating in air atmosphere. The electrode of deactivated CuO_x/AC catalyst after treatment maintains a high reversible capacity of 621.3 mAh·g^{-1} at 100 mA·g^{-1} after 100 cycles, which is superior to the fresh CuO_x/AC catalyst (~446.1 mAh·g^{-1}) and deactivated CuO_x/AC catalyst without treatment (~420.7 mAh·g^{-1}). From this result of excellent electrochemical performances, this work provides a new line to recycle catalyst CuO_x/AC composites from catalyzed synthesis DMC to LIBs anodes, and furthermore, transfer "waster catalyst" into "energy storage material".

2. EXPERIMENTAL

2.1. Activating treatment of AC

The active carbon with specific surface areas of 1409.3 m^2 g^{-1} was commercially available (Xinsen Chemical Industry Co. Ltd. China) and refluxed in oil bath at 70 ^{o}C by 6 mol L^{-1} HNO$_3$ for 6 h.

Then the powder was washed by deionized water until pH 7, and finally dried at 100 ^{o}C overnight. Subsequently, nano-sized copper oxides can be distributed uniformly on the surface and channels of the active carbon.

2.2. Synthesis of CuO$_x$/AC catalysts

For comparison, we fabricated fresh CuO$_x$/AC compounds before employed to catalytic synthesize DMC. 4.2 g copper nitrate trihydrate (Cu(NO$_3$)$_2$·3H$_2$O) was dissolved in deionized water with continuous stirring until blue transparent solution formed. Then 4.42 g pretreated AC was added into the Cu(NO$_3$)$_2$ solution with a mass ratio (Cu : AC=1:4), note that the mass of Cu refers to that of Cu element. After vigorous stirring for 6 hours at room temperature and dried at 100 ^{o}C overnight, the precursor was calcined at 350 ^{o}C for 4 h in the flowing nitrogen atmosphere. The black product with various Cu valence states was obtained, marked as C-1. The fresh catalyst was packed in the tubular reactor and placed in the middle of reactor furnace. Then methanol of 3 mL h^{-1} was imported by means of a constant-flux pump and vaporized in the pre-heater, following mixed carbon monoxide and oxygen together, and then enclosed into the catalyst bed to be catalyzed for oxidative carbonylation to DMC. After this process, the deactivated catalyst without treatment was obtained, which was marked as C-2. To raise the content of CuO, the deactivated CuO$_x$/AC catalyst was heat-treated at 100 ^{o}C overnight and noted as C-3.

2.3. Characterization

Crystal phase of the compounds were examined by X-ray Diffraction (XRD, Rigaku D/max 2500) at 40 kV and 100 mA, with Cu Kα radiation (λ=1.541 Å) and scanning range from 30° to 80° (0.02° per step). Morphology was characterized by High Resolution Transmission Electron Microscopy (HR-TEM, GG314-JEM-2100F) at 200 kV. The valence states of Cu element were detected by X-ray photoelectron spectroscopy (XPS, ESCA Lab220i-XL) and H$_2$-Temperature Programmed Reduction (H$_2$-TPR, Autochem II 2920).

For the TPR experiments, 25 mg of sample was placed into a U-shape quartz reactor, with argon flowing (20 mL min^{-1}, 2 h) at 200 ^{o}C to remove moisture in the reactor. After cooling down, the gas was switched to 10% H$_2$ in argon flow (20 mL min^{-1}), and sample was heated from room temperature to 900 ^{o}C with a heating rate of 20 ^{o}C min^{-1}. The amount of H$_2$ consumption during reduction was calculated by the thermal conductivity detector.

The BET surface areas of CuO$_x$/AC catalysts were determined by N$_2$ adsorption-desorption instruments apparatus (BeiShiDe 3H-2000 PS2), and the pore size was calculated by using Barret Joyner Halender (BJH) method, which is the adsorption brand of nitrogen isotherm.

2.4. Electrochemical test

Electrochemical performances of resulted composites were performed using coin-type cells.

The test cells were assembled in an argon filled glove box, where the moisture content and oxygen levels were controlled below 0.5 ppm (25 ^{o}C). The working electrodes were made by a slurry coating procedure, and fabricated by active materials, conductive agent (acetylene black) and binder (polyvinylidene fluoridesin N-methyl pyrrolidinone) in a weight ratio of 70: 20: 10. The slurry was coated onto a copper foil substrate and dried at 100 ^{o}C for 12h in vacuum. Li foil was used as both counter electrode and reference electrode. 1 M $LiPF_6$ in mixture of ethylene carbonate (EC) and dimethyl carbonate (DMC) (1:1 vol%) was used as the electrolyte, and a polypropylene (PP) microporous film was used as the separator. The electrode capacity was measured by a galvanostatic discharge-charge method at a current density of 100 mA·g^{-1} using a battery analyzers (LAND, Wuhan, China), then rate measurement was tested at different current density (100 mA·g^{-1}, 200 mA·g^{-1}, 500 mA·g^{-1}, 1000 mA·g^{-1}, 2000 mA·g^{-1}, 100 mA·g^{-1}) with 10 charge-discharge cycles each step. Cyclic voltammetry (CV) was tested on Electrochemical Workstation (CHI 660E, Chen-hua, Shanghai, China) with the voltage ranged from 0.01 to 3V (vs. Li$^+$/Li), and scan rate of CV is 0.1 mV·s^{-1}.

3. RESULTS AND DISCUSSION

The phase compositions of three samples were examined by XRD at room temperature with results shown in Fig. 1.
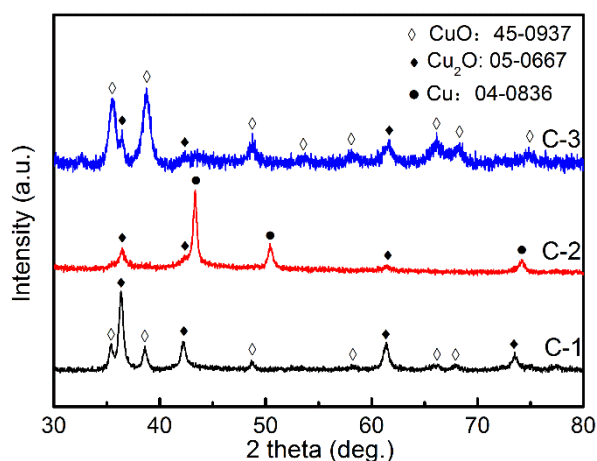

Figure 1. XRD patterns of fresh catalyst (C-1) and deactivated catalyst without treatment (C-2) and after heat treatment (C-3).

The XRD pattern of fresh catalyst (C-1) suggested that the product included different forms of copper element: Cu_2O and CuO. Additionally, the Cu_2O remains in the majority, which shows a cubic crystal structure (JCPDS card 05-0667). Its main diffraction peaks appear at 2θ=36.296°, 42.297°, 61.344°, 73.526° corresponding to (111), (200), (220), (220) and (311) planes, respectively. The remanent diffraction peaks refer to CuO with monoclinic phase (JCPDS card 45-0937). In the fresh catalyst, high concentration of Cu_2O nanoparticles with small grain size was formed by carbothermic

reduction under protective atmosphere. It is the Cu_2O phase that plays as the active center in the reaction of oxidative carbonylation of methanol to catalyzed synthesis DMC [12, 13]. In general, the copper particles growth and change of copper's chemical state, occur along with catalysis process and are the main reason for the deactivation of supported copper catalysts [14]. The deactivated catalyst without treatment (sample C-2) shows plenty of copper elementary substance (Cu^0) with cubic phase (JCPDS card 04-0836), corresponding to the lattice planes of (111), (200) and (220), and minority of Cu_2O and CuO. The XRD pattern of deactivated catalyst after heat treatment (sample C-3) shows that the overwhelming majority of copper element exists as bivalence (CuO). It is obvious that the simple heat-treatment under air atmosphere could promote the oxidation of Cu species effectively. Crystallite sizes are calculated by Scherrer equation to be 8.1 nm, 12.8 nm and 18.7 nm for the C-1, C-2 and C-3 samples, respectively. The results were similar with other Cu based catalyst [11]. Considering that the theoretical electrochemical capacitance of CuO is higher than that of Cu_2O and Cu, heat-treatment can accelerate the oxidation of Cu and Cu_2O, and more CuO may enhance Li-ion specific storage for the Cu/AC catalyst.

When the CuO_x/AC catalysts were used in the reaction to synthesize DMC, there are only CH_3OH, CO and O_2 which involved in the reaction. Unlike the conventional CuCl catalyst with Cl ion, the CuO_x/AC catalyst will not lead to equipment corrosion [15]. Additionally, low reaction temperature (~130 ^{o}C) is another factor to make sure that the CuO_x/AC catalyst cannot be polluted in the catalytic process of synthesis DMC. In the process, the main product is DMC and other by-products are dimethyl ether (DME), methylal (DMM) and methyl formate (MF). The boiling point for the products above are 90.1 ^{o}C (DMC), -24.9 ^{o}C (DME), 42.3 ^{o}C (DMM), 32 ^{o}C (MF), respectively. That is to say, all the organic products have been volatilized after heat treatment (100 ^{o}C, overnight, air atmosphere) and slurry drying stage (100 ^{o}C, 12h, vacuum). Therefore, only C, O, Cu elements remained in the deactivated catalyst when employed as LIBs' electrodes.
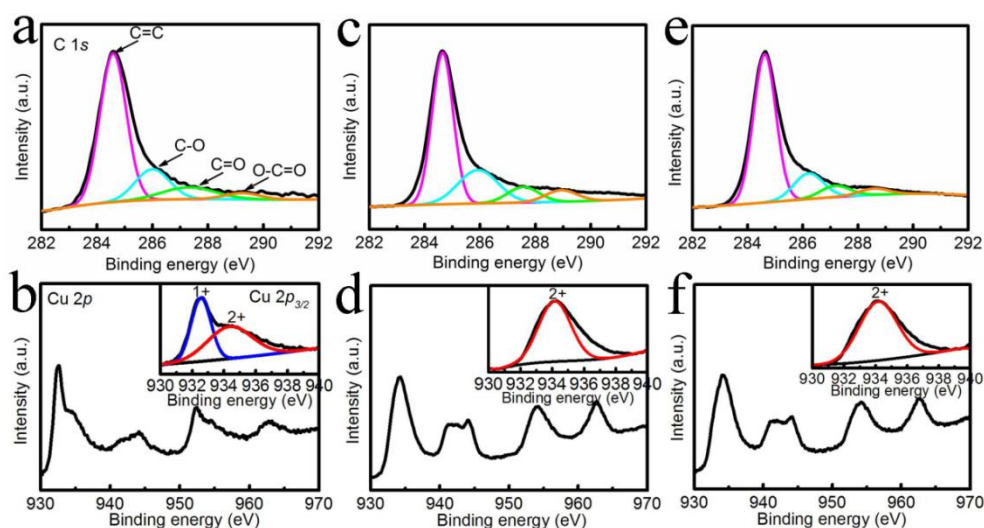

Figure 2. the C 1*s* and Cu 2*p* XPS spectra of C-1 (a, b), C-2 (c, d), C-3 sample (e, f) and the inset shows Cu 2$p_{3/2}$ XPS spectrum.

In order to investigate the oxygenated groups on the surface of three samples, the C 1*s* and Cu 2*p* XPS spectra of C-1, C-2 and C-3 sample were collected and displayed in the Fig. 2. From Fig. 2a, c, e, the C 1*s* results can be deconvoluted into four components consistent with following carbon functional groups: C=C (284.6 eV sp^2 carbon atoms), C-O (286.2 eV), C=O (287.6 eV) and O-C=O (289.1 eV) [16]. For three samples with different treatment methods, the carbon functional groups have no obvious change.

Due to active performance of functional groups, they can easily react with Li-ion, and thus improve energy storage properties of anode materials [17]. Moreover, the functional group can enhance the redox reaction of copper oxides [18]. Considering that the position of Cu 2*p* emerges at 934.6 eV for Cu^{2+} [19], the main peak is fitted and clearly demonstrates mixed valence state of Cu (divalent) in sample C-1, C-2 and C-3. This conclusion is constant with the XRD result. But for the sample C-2 and C-3, Cu 2*p* spectra demonstrate no obvious evidence of Cu_2O on the surface for the deactivated catalyst.

However, usually XPS technique can only reflect the information on the surface with depth of 3-5 nanometers. The insertion/deinsertion of Li-ion is not only restricted to surface of active materials during charge/discharge process, and we need to study the changes of element valence state insides the compounds. H_2-Temperature-Programmed Reduction (H_2-TPR) is a powerful tool to investigate the valence states of metal oxides, which is evaluated by the amount of H_2 consumption during the reduction process. The H_2-TPR profiles obtained from C-1, C-2 and C-3 samples are shown in Fig. 3. The profiles of C-1, C-2 and C-3 were characterized by reduction peaks at various irradiation temperatures (150-300 ^{o}C, 300-500 ^{o}C). The first peak can be deconvoluted into peaks α_1 and α_2, which are ascribed to the reduction of the well-dispersed CuO [20] and the Cu^{2+} immobilized onto the functional groups of AC [21], respectively. The second peak, marked as β, can be assigned to the formation of Cu_2O phases on the active carbon support. The peak γ is not considered, because it is ascribed to reduction of the surface oxygenic functional groups of active carbon [22]. The appearance of three H_2-TPR characteristic peaks supports the XRD results above.
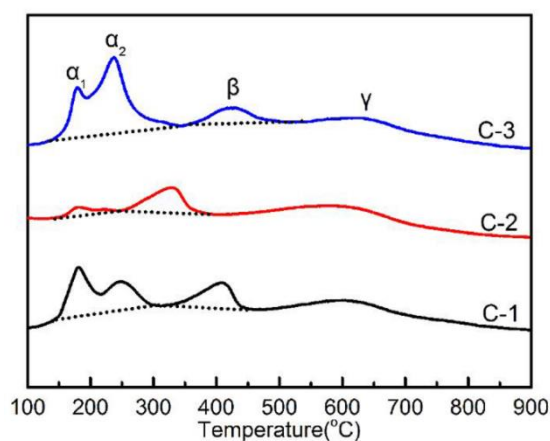

Figure 3. H_2-TPR profiles of the CuO_x/AC catalysts.

For the fresh catalyst (C-1), CuO and Cu_2O exist on the surface and inside the body of the nanoparticles. As presented in the XRD result, Cu element in the deactivated catalyst (C-2) was composed of the majority of elementary Cu and minority of CuO and Cu_2O. Moreover, it is known that elementary Cu can't be reduced during H_2 reduction reaction. Therefore, the characteristic peaks of H_2-TPR profile representing CuO and Cu_2O are quite weak, especially the CuO phase. After simple heat treatment, the contents of CuO have greatly increased (sample C-3). The amount of H_2 consumption of CuO in C-3 sample (~3.9834 mmol g^{-1}) is higher than that of C-1 (~2.3448 mmol g^{-1}) and C-2 sample (~0.2435 mmol g^{-1}), but the amount of H_2 consumption of Cu_2O in C-3 sample (~0.8108 mmol g^{-1}) is lower than that of C-1 (~1.1331 mmol g^{-1}) and C-2 sample (~1.1479 mmol g^{-1}). The combination of XPS result and peak β in H_2-TPR profile declare the existence of monovalent copper in the sample C-3, but only in the interior of the nanoparticles not on the surface. This conclusion is supported by the XRD and XPS analysis, and may indicate better electrochemical capacity for C-3 sample compared with the C-1 and C-2 samples. Additionally, reduction peaks of sample (C-3) shifted toward to higher temperature compared with other two samples. The main reason for this is that the binding force between copper oxide nanoparticles and active carbon support goes stronger [19]. This would cause better structure stability for the material during the charge/discharge process as electrode.

Nitrogen adsorption-desorption isotherms technique was carried out to specific surface area of AC, C-1, C-2 and C-3 samples, and the corresponding pore size distributions were calculated by the BJH method.
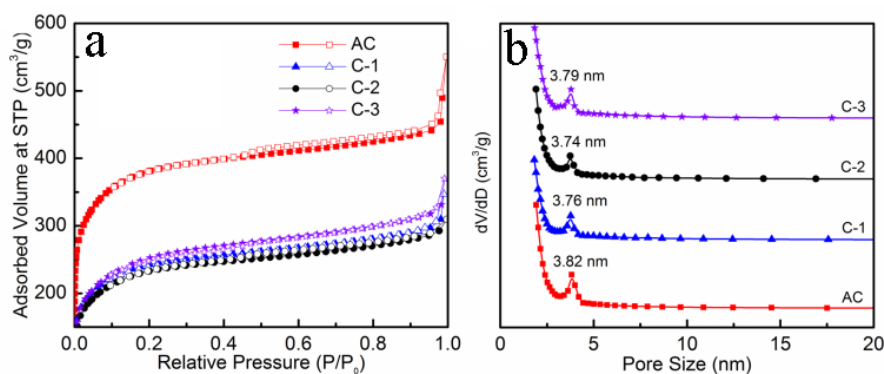

Figure 4. Nitrogen adsorption-desorption of (a) isotherms of samples. (b) the corresponding BJH pore size distribution curves.

Table 1. Textural parameters of AC, C-1, C-2 and C-3 samples

Samples	S_{BET} (m^2 g^{-1})	Pore volume (cm^3 g^{-1})	Pore size BJH (nm)
AC	1409.3	0.6794	3.82
C-1	871.8	0.4308	3.76
C-2	823.9	0.4001	3.74
C-3	905.1	0.4971	3.79

As shown in Fig. 4(a), the isotherms of three samples exhibit a typical IUPAC type IV characteristic with a distinct H4 hysteresis loop resulted from capillary condensation [23], indicating the presence of micropore and mesopore in materials. The BET specific areas are calculated to be 1409.3 $m^2 g^{-1}$, 871.8 $m^2 g^{-1}$, 823.9 $m^2 g^{-1}$ and 905.1 $m^2 g^{-1}$, respectively. Fig. 4(b) shows the corresponding pore size distributions by BJH analysis. The average pore volume is about 0.6794 $cm^3 g^{-1}$ for active carbon. After the copper particles incorporating into the AC support, an obvious drop in pore volume was observed for C-1, C-2 and C-3 samples (Table 1). While, the most probable apertures for three samples haven't changed and still hold at around 3.7 nm, implying the mesoporous architecture of AC host is not damaged after catalytic reaction and subsequent heat treatment.

The morphologies and microstructures of the three samples were further investigated using TEM. Active carbon presents porous structure with a BET specific surface area of 1409.3 $m^2 g^{-1}$. In Fig.5(a), it is clearly observed that the CuO_x nanoparticles are distributed uniformly over the surface of active carbon, without any nanoparticle aggregations.
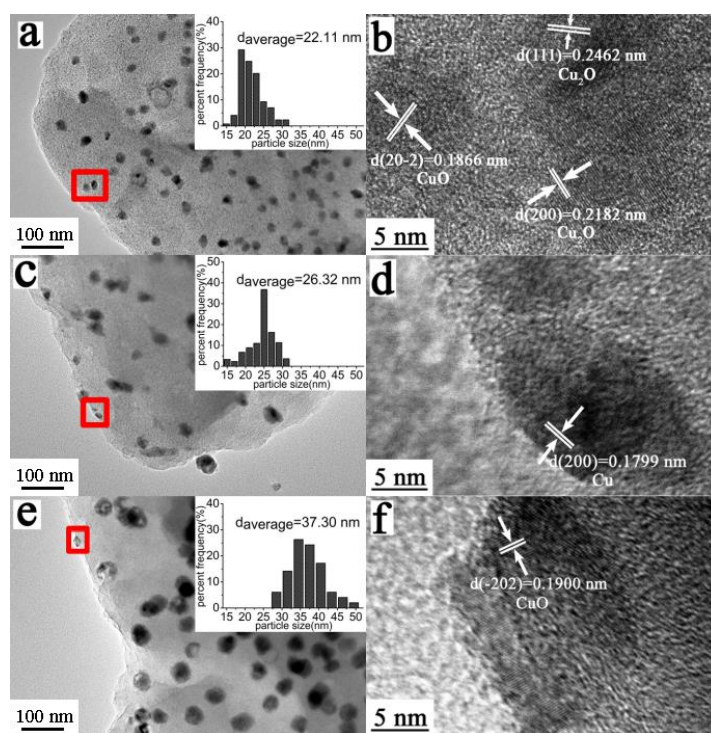

Figure 5. TEM images of CuO_x/AC (a, b: sample C-1. c, d: sample C-2. e,f: sample C-3.).

The average diameter of copper oxide is figured out to be about 22.11 nm for the fresh catalyst (C-1) by Nano Measure software. The copper based catalysts suffered from the copper particles growth and change of copper valence state after deactivation [14]. For C-2 and C-3 samples, the obvious size growth of copper particles is observed as shown in Fig .5 (c) and Fig. 5 (e), with copper particles size about 26.32 nm and 37.30 nm, respectively. The HR-TEM images were used to further understand the dimensionality of the CuO_x nanoparticles. Fig.5 (b) displays a lattice resolved HR-TEM image of C-1 sample. The distance between adjacent lattice fringes were measured about 0.1866 nm, 0.2182 nm and 0.2462 nm, which are corresponding well to the *d*-spacing of the (20-2), (200) fringes of CuO and

(111) fringes of Cu_2O. The HR-TEM images of the C-2 and C-3 samples are illustrated in Fig.5(d) and Fig.5(e), and inter planar spacing (0.1799 nm) and (0.1900 nm) are observed in good agreement with the spacing of the (200) crystal plane of the Cu cubic structure and the (-202) crystal plane of the CuO monoclinic structure. These results are consistent with the XRD observations.
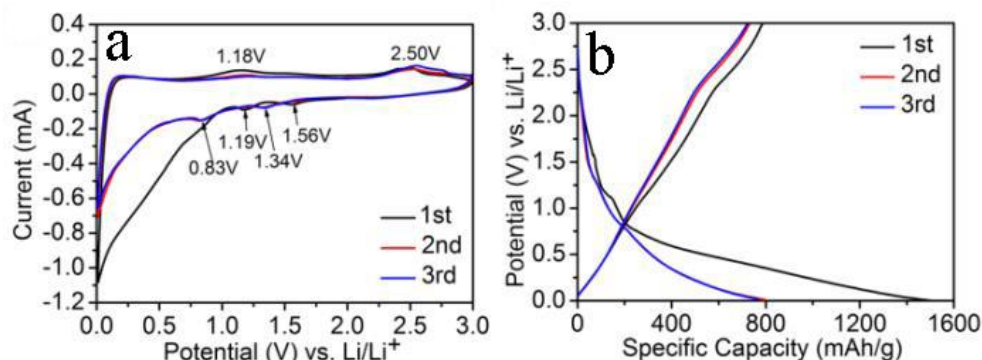

Figure 6. (a) CV curves of C-1 electrode at a scan rate of 0.1 mv·s^{-1} from 0.01-3 V. (b) Typical galvanostatic charge/discharge curves of C-3 electrode between 0.01 V and 3 V vs. Li$^+$/Li at constant current density of 100 mA·g^{-1}.

To demonstrate the Li-ion insertion/extraction reactions of C-3 sample, the cyclic voltammetry (CV) curve was measured at a scan rate of 0.1 mV·s^{-1} and shown in Fig.6(a), those of C-1 and C-2 samples are shown in Fig. S1 (see supporting information). There are two cathodic peaks located at 1.19 and 1.56 V (vs. Li$^+$/Li) in the first cathodic scan process. The reduction peaks related to the electrochemical lithiation reaction from CuO/Cu$_2$O into Cu and amorphous Li$_2$O with the formation of an intermediate phase of a Cu$^{II}_{1-x}$Cu$^{I}_x$O$_{1-x/2}$(0≤x≤0.4) solid solution [24]. In the first anodic scan process, there are two anodic peaks which located around 1.18 and 2.56 V during the charge process, with oxidation peak corresponding to the major conversion from Cu to Cu$_2$O and partially CuO during the delithiation process [25, 26]. The mechanism of reaction are follow as: 2CuO + 2Li$^+$ + 2e$^-$ ←→Cu$_2$O + Li$_2$O; Cu$_2$O + 2Li$^+$ + 2e$^-$←→2Cu + Li$_2$O, these completely reversible reaction can conduce to extra capacity. The CV curve of innital cycle is distinctly different from those of squential cycles, demonstrating a great quantity of irreversible capacity decaying in the first cycle. During the following cycles, two cathodic peaks located near 0.83 and 1.34 V and also can be assigned to the CuO/Cu$_2$O reduction to Cu. The anodic peaks showed the same potentials and were relatve to the metal Cu oxidation to Cu$_2$O/CuO. Compared with the inital cycle, the cathodic potentials of sucessive cycles had shifted due to the polarization of electrode [27]. For CV curves, the areas enclosed from inital cycle to second cycle present a decline, indicating that the electrode reaction with enhanced reversibility. Meanwhile, the individual peak intensity and integral area almost overlapped in the following cycles, confirming that the reversible capacity gradually stablized after the first cycle. Besides, the CV curvies of C-1 and C-2 samples are similar with that of C-3 sample, declaring the similar mechanism of reversible oxidation-reduction reactions.

The electrochemical performance of the C-3 composite was evaluated by galvanostatic charge/discharge cycling and shown in Fig.6 (b). The curves of C-3 sample for 1st, 2nd and 3rd cycles

were recorded in the voltage range of 0.01-3.0 V (vs. Li$^+$/Li). In the first discharge cycle, there are two obvious sloping potential ranges: 1.7-1.5 and 1.5-1.0 V, demonstrating the crystal structure destruction (amorphization), and the formation of Cu/Li$_2$O and the decomposition of electrolyte, which are in good agreement with three cathodic peaks in the above CVs. In the second discharge curve, the potential range appears at 1.5-1.0 and 1.0-0.5 V, and narrows compared with the first discharge curve. This result leads to the loss of discharge capacity. Meanwhile, the change in potential ranges and irreversible capacity before the first two discharge cycles are fit with the observation in CVs above. During the following discharge process, the curve shapes have little change apart from narrowing. Upon the charging process, a plateau located at near 2.4 and 1.2 V can be clearly marked during all charge cycles. Also, the curves of C-1 and C-2 samples are well match with their CVs results, and they have analogous variation tendency to C-3 sample. The reaction mechanism responding to profiles of C-1 and C-2 curves are similar with that of C-3 sample. The result of C-3 sample demonstrates CuO$_x$/AC catalyst suitable as a promising candidate for LIBs anode material with high reversible capacities.
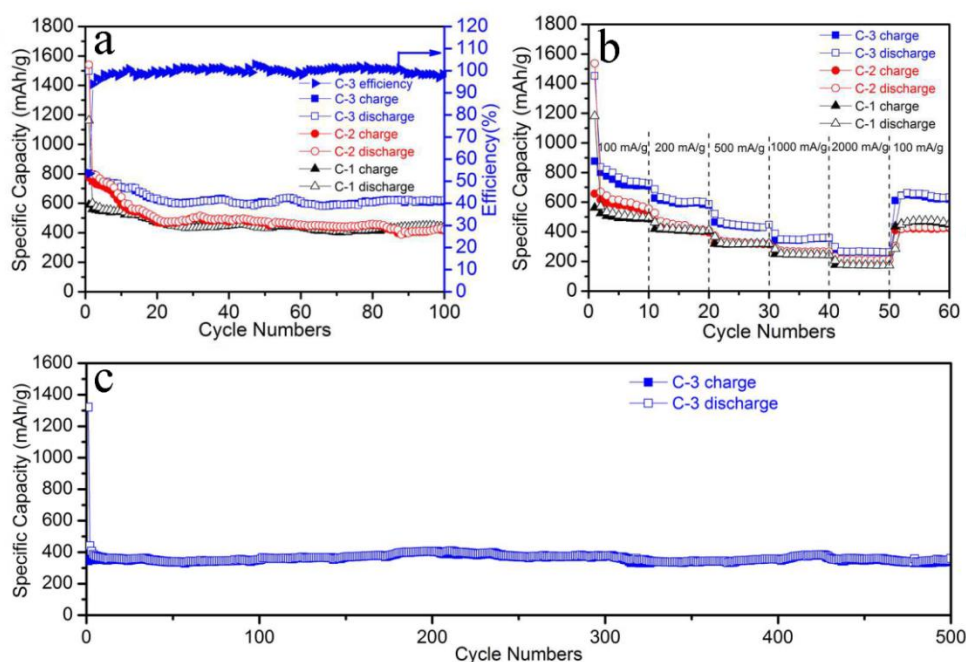

Figure 7. (a) Cycling performances of C-1, C-2, C-3 samples between the potential ranges of 0.01-3 V at a current density of 100 mA·g^{-1}. (b) Electrochemical performance at various current densities. (c) Cycling performance at the current densities of 1A·g^{-1} of C-1 electrode.

To study the potential application of the deactivated catalyst after heat-treatment (sample C-3) as a lithium-ion battery anode, galvanostatic discharge/charge test was carried out at a current density of 100 mA·g^{-1}. Fig. 7(a) displays specific capacities and Coulombic Efficiency data of the sample C-3 in regard to the cycling numbers. Meanwhile, the sample C-1 and sample C-2 were also measured under same condition, and the cycling capacity of AC is shown in Fig. S2 (see supporting information). The initial discharge/charge specific capacities have exceeded theoretical capacity, which

can be ascribed to the catalytic decomposition of electrolyte solvents. The irreversible capacity decaying during first cycle is mainly caused by inevitable formation of a solid electrolyte interface (SEI) layer, resulting from chemical reaction of Li with ethylene carbonate, consuming much Li. Besides, the crystal structure destruction is another factor, which results from metal particles embedded into the Li_2O matix in the first cycle. The C-3 electrode discharge capacity declined slowly after 2nd cycle and then rose slightly after 30th cycle reaching a stable level of 621.3 mAh·g^{-1} by the 100th cycle, with corresponding Coulombic Efficiency stable at the value of nearly 100%. The gradual increase during the cycling is ascribed to the SEI absolutely develops and become stable during subsequently cycles. Because that it prevents excessive solvent cointercalation and uses as Li conductor and enables facile Li cycling [28, 29]. Furthermore, the stable lithium oxide (Li_2O) is electrochemically inactive and cannot be decomposed to the metal and oxygen, thereby buffering volume variation and capacity fading by maintaining the electrode intergity. It also provides ionically conducting medium for Li^+ migration and promotes large and reversible capacities. The active carbon might be beneficial for more electrolyte to contact with active materials, bringing into the capacity augments during the Li-ion insertion/extraction processes. Also, the porous structure can act as elastic buffer to ease the mechanical stress by volume expansion. Obviously, the discharge capacity of C-3 electrode is higher than AC (~352.9 mAh g^{-1}), C-1 electrode (~446.1 mAh·g^{-1}) and C-2 electrode (~420.7 mAh·g^{-1}) after 100th cycle, indicating excellent cycling performance of the CuO_x/AC catalysts as LIBs' electrode. Despite the size of C-3 particles increased after heat treatment, more Cu and Cu_2O were oxidized into CuO and the content of CuO increased a lot in deactivated catalyst. Heat-treatment can result in better interparticles contact and stronger binding force, which was proved by H_2-TPR above.

Table 2. The comparisons of specific capacities of different CuO-based electrodes.

materials	current density (mA g^{-1})	cycles	specific capacity (mAh g^{-1})	references
CuO microsphere	67	50	429	[24]
CuO nano-needle arrays	67	50	441	[8]
CuO/graphene composite	67	50	583.5	[29]
CuO/C nanocapsules	100	50	628.7	[28]
CuO_x/AC catalyst	100	100	621.3	This work
CuO/Cu composite	100	110	706	[32]

Thus the reversible capacity of C-3 sample is higher than sample C-1 and C-2. Compared with precious research, the reversible capacity of C-3 electrode is comparable with onion-like carbon coated CuO/C nanocapsules [30], and superior to the CuO/graphene composite [31] and CuO microspheres [24], but lower than CuO/Cu composite [32]. However, these copper based anode materials were

prepared under complex condition (e.g. arc-discharge, hydrothermal method). The CuO_x/AC anode originates from deactivated catalyst, providing an environment-friendly course with high production and low cost. Although the theoretical capacity is low, Cu_2O can provide stable reversibility in electrochemical reaction for the hybrid material [33]. Therefore, the cycling property of C-3 sample is more stable than CuO nanoparticle-aggregated microsheets on Cu foil [32]. As discussed above, the theoretical capacity of CuO is higher than that of Cu_2O, and the C-3 sample displays excellent electrochemical performance. As described in the literatures, the detailed comparison of specific capacities of different CuO-based electrodes are shown in Table 2.

Compared with these materials, the catalyst C-3 not only shows high reversible capacity but also low time-cost and simple operating procedures.

To further understand the electrochemical performance of C-3 electrode, we also tested the rate performance under varying current densities as is shown in Fig.7(b). The current densities were gradually increased from 0.1 $A \cdot g^{-1}$ to 2 $A \cdot g^{-1}$ and then returned to 0.1 $A \cdot g^{-1}$, including 10 discharge/charge cycles in each step. The discharge capacity at 0.2, 0.5, 1 and 2 $A \cdot g^{-1}$ is 601.4, 440.5, 347.5 and 258.6 $mAh \cdot g^{-1}$, respectively. It is noticeable that the current density increased with a corresponding capacity decreasing. Although the capacity was not fully recovered relative to the first 10 cycles, a discharge capacity recovered as high as 629.9 $mAh \cdot g^{-1}$ when the current density went back to 0.1 $A \cdot g^{-1}$, illustrating that irreversible capacity occurred during electron and lithium-ion transfer and electrochemical reaction process. This result predicted that C-3 electrode has ability of bearing high current rates and has good cycling stability. By comparison, the rate property of C-3 electrode is much better than that of C-1 electrode and C-2 electrode. Due to importance of the charge/discharge performance under high current density for many practical apparatus (e.g. electric vehicles and mobile phone) [34], we further investigated the cycle behavior of C-3 electrode at current density of 1 $A \cdot g^{-1}$. As shown in Fig.7(c), the discharge capacity reached 359.6 $mAh \cdot g^{-1}$ even after 500 cycles with nearly 100% retention after the first cycle.

The discharge capacity of fresh catalyst is higher than the theoretical value. This phenomenon presented in other transition-metal oxides anodes such as CuO [32], Co_3O_4 [35], Fe_2O_3 [36], MnO [37]. The reason for high property of CuO_x/AC material in this work, is the fine stability nanostructure and the reversible electrochemical lithium ion insertion/extraction process. Before supported Cu species, AC was pretreated by HNO_3, leading to more oxygen functional groups on the surface. They can act as active sites, significantly facilitating the oxidation and reduction reaction of Cu/CuO_x, which involves the transfer of oxygen atom [17]. Besides, CuO_x nanoparticles with small size were uniformly distributed on the surface of AC and can shorten the Li^+ diffusion path, making the Li^+ transfer quickly and efficiently at the electrode/electrolyte interface and enhance the kinetics of conversion reactions. CuO_x/AC nanostructure can also restrain from particle pulverization/aggregation and the cracking of the electrode, assure mechanical cohesion and provide extra capacity at low potential by a ''pseudo-capacitance-type behavior'' during continuous charge-discharge process [30]. Furthermore, the strong binding force between copper oxides nanoparticles and active carbon cause better structure stability during the charge/discharge process. Additionally, the interaction of CuO and Cu_2O has effects in the better reversibility in electrochemical reaction.

4. CONCLUSIONS

In summary, we employed the CuO_x/AC catalyst as LIBs' anodes. The investigation of valence states by XPS and H_2-TPR demonstrates mixed valence states of Cu inside and on the surface of fresh catalyst. After simple heat-treatment, the electrode of deactivated catalyst performs an excellent circulation capacity with a reversible capacity of 621.3 mAh·g^{-1} at the current density of 100 mA·g^{-1} after 100 cycles, and remains a capacity of 359.6 mAh·g^{-1} after 500 cycles at 1 A·g^{-1}. This is attributed to uniform particles distributed on the porous active carbon, and important coordination ability of AC, cupric and cuprous oxides. In addition, the binding force between CuO_x particles and AC support can enhance structure stability in the cycle process. The oxygen-containing functional groups have effects on catalyzing redox reaction, and increase active sites for delithiation/lithiation. This facile strategy may provide a feasible route for the large-scale manufacture of high-powered and eco-friendly electrode materials, which can be widely used in industry. And more importantly, this indicates the application of this material not only in catalyzed synthesis DMC but also in negative electrode of lithium-ion battery.
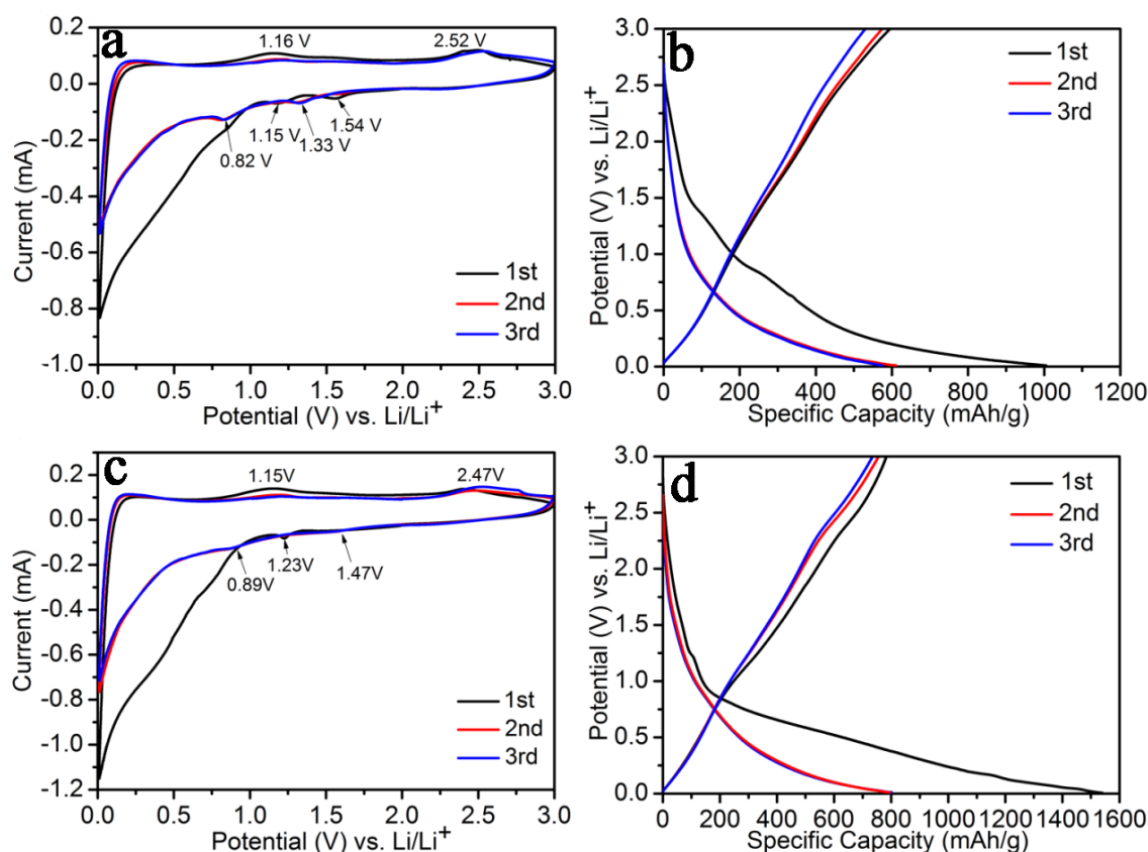
SUPPORTING INFORMATION:

Fig. S1 CV curves of C-1 and C-2 electrode at a scan rate of 0.1 mv·s^{-1} from 0.01-3 V (a,c). Typical galvanostatic charge/discharge curves of C-1 and C-2 electrode between 0.01 V and 3 V vs. Li^+/Li at constant current density of 100 mA·g^{-1} (b,d).

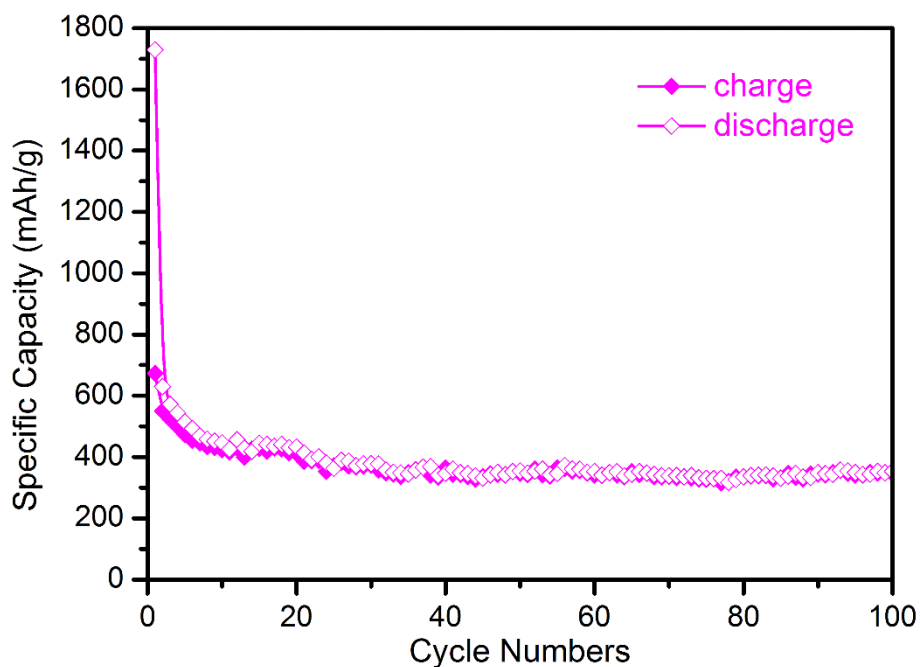**Fig. S2** Cycling performance of AC sample between the potential ranges of 0.01-3V at a current density of 100 mA·g^{-1}.

References

1. J. Dahn, T. Zheng, Y. Liu, J. Xue, *Science*, 270 (1995) 590.
2. Y. Zhao, Y. Zhang, H. Zhao, X. Li, Y. Li, L. Wen, Z. Yan, Z. Huo, *Nano Research*, 8 (2015) 2763-2776.
3. P. Roy, S.K. Srivastava, *J. Mater. Chem. A*, 3 (2015) 2454-2484.
4. C. Zhu, D. Chao, J. Sun, I.M. Bacho, Z. Fan, C.F. Ng, X. Xia, H. Huang, H. Zhang, Z.X. Shen, G. Ding, H.J. Fan, *Adv. Mater. Interfaces*, 2 (2015).
5. X. Hu, C. Li, X. Lou, Q. Yang, B. Hu, *J. Mater. Chem. A*, (2017).
6. H. Yin, X.-X. Yu, Q.-W. Li, M.-L. Cao, W. Zhang, H. Zhao, M.-Q. Zhu, *J. Alloy. Compd.*, 706 (2017) 97-102.
7. W. Yang, J. Wang, W. Ma, C. Dong, G. Cheng, Z. Zhang, *J. Power Sources*, 333 (2016) 88-98.
8. J. Xiang, J. Tu, J. Zhang, J. Zhong, D. Zhang, J. Cheng, *Electrochim. Commun.*, 12 (2010) 1103-1107.
9. D. Ortiz, V. Steinmetz, D. Durand, S. Legand, V. Dauvois, P. Maitre, S. Le Caer, *Nat. commun.*, 6 (2015) 6950.
10. P. Poizot, S. Laruelle, S. Grugeon, L. Dupont, J. Tarascon, *Nature*, 407 (2000) 496-499.
11. J. Ren, W. Wang, D. Wang, Z. Zuo, J. Lin, Z. Li, *Appl. Catal. A: General*, 472 (2014) 47-52.
12. B. Yan, S. Huang, S. Wang, X. Ma, *ChemCatChem*, 6 (2014) 2671-2679.
13. R. Zhang, L. Song, B. Wang, Z. Li, *J. Comput. Chem.*, 33 (2012) 1101-1110.
14. R.G. Wall, Pinole, *CA US* 4 (1978) 021.

15. S. Huang, B. Yan, S. Wang, X. Ma, *Chem. Soc. Rev*., 44 (2015) 3079-3116.
16. B. Xiong, Y. Zhou, Y. Zhao, J. Wang, X. Chen, R. O'Hayre, Z. Shao, *Carbon*, 52 (2013) 181-192.
17. H. Fujimoto, A. Mabuchi, K. Tokumitsu, T. Kasuh, *J. Power Sources*, 54 (1995) 440-443.
18. W. Li, J. Liu, C. Yan, *Carbon*, 49 (2011) 3463-3470.
19. G. Zhang, Z. Li, H. Zheng, T. Fu, Y. Ju, Y. Wang, *Appl. Catal. B: Environmental,* 179 (2015) 95-105.
20. J.L. Figueiredo, *J. Mater. Chem*. A, 1 (2013) 9351-9364.
21. D.A. Svintsitskiy, T.Y. Kardash, O.A. Stonkus, E.M. Slavinskaya, A.I. Stadnichenko, S.V. Koscheev, A.P. Chupakhin, A.I. Boronin, *J. Phys.Chem*. C, 117 (2013) 14588-14599.
22. J. Ren, M. Ren, D. Wang, J. Lin, Z. Li, *J. Therm. An. Calorim.*, 120 (2015) 1929-1939.
23. F. Wu, R. Huang, D. Mu, X. Shen, B. Wu, *J. Alloy. Compd*., 585 (2014) 783-789.
24. C. Wang, D. Higgins, F. Wang, D. Li, R. Liu, G. Xia, N. Li, Q. Li, H. Xu, G. Wu, *Nano Energy*, 9 (2014) 334-344.
25. A. Debart, L. Dupont, P. Poizot, J. Leriche, J. Tarascon, *J. Electrochem. Soc*., 148 (2001) A1266-A1274.
26. X. Wang, D.-M. Tang, H. Li, W. Yi, T. Zhai, Y. Bando, D. Golberg, *Chem. Commun*., 48 (2012) 4812-4814.
27. Z. Xing, Z. Ju, J. Yang, H. Xu, Y. Qian, *Electrochim. Acta*, 102 (2013) 51-57.
28. A.S. Arico, P. Bruce, B. Scrosati, J.-M. Tarascon, W. Van Schalkwijk, *Nat. Mater*., 4 (2005) 366-377.
29. P. Verma, P. Maire, P. Novák, *Electrochim. Acta*, 55 (2010) 6332-6341.
30. X. Liu, N. Bi, C. Feng, S.W. Or, Y. Sun, C. Jin, W. Li, F. Xiao, *J. Alloy. Compd*., 587 (2014) 1-5.
31. Y.J. Mai, X.L. Wang, J.Y. Xiang, Y.Q. Qiao, D. Zhang, C.D. Gu, J.P. Tu, *Electrochim. Acta*, 56 (2011) 2306-2311.
32. K. Chen, D. Xue, S. Komarneni, *J. Power Sources,* 275 (2015) 136-143.
33. X. Zhou, J. Shi, Y. Liu, Q. Su, J. Zhang, G. Du, *J. Alloy. Compd*., 615 (2014) 390-394.
34. C. He, S. Wu, N. Zhao, C. Shi, E. Liu, J. Li, *ACS Nano*, 7 (2013) 4459-4469.
35. L. Wang, Y. Zheng, X. Wang, S. Chen, F. Xu, L. Zuo, J. Wu, L. Sun, Z. Li, H. Hou, Y. Song, *ACS Appl. Mater. Interfaces*, 6 (2014) 7117-7125.
36. W. Xiao, Z. Wang, H. Guo, Y. Zhang, Q. Zhang, L. Gan, *J. Alloy. Compd*., 560 (2013) 208-214.
37. J. Zang, H. Qian, Z. Wei, Y. Cao, M. Zheng, Q. Dong, *Electrochim. Acta,* 118 (2014) 112-117.